

Contents lists available at [ScienceDirect](https://www.sciencedirect.com)

Journal of Sound and Vibration

journal homepage: www.elsevier.com/locate/jsvi

A 3D-printed quasi-zero-stiffness isolator for low-frequency vibration isolation: Modelling and experiments

Lei Xiao, Xiang Sun, Li Cheng, Xiang Yu^{*}*Department of Mechanical Engineering, The Hong Kong Polytechnic University, Hong Kong, China*

ARTICLE INFO

Keywords:

Vibration isolation
Quasi-zero stiffness
3D printing
Nonlinear damping
Damping identification

ABSTRACT

Quasi-zero-stiffness (QZS) isolators have shown great promise for low-frequency vibration isolation, thus outperforming conventional linear isolators. However, the hardening behavior typically exhibited in QZS isolators can deteriorate the isolation performance at high excitation amplitudes. To tackle this problem, utilizations of inherent material damping in soft resin offer a feasible way to counteract the hardening effect. This paper proposes a continuous QZS isolator, which can be readily fabricated by three-dimensional (3D) printing using soft resin. QZS properties are achieved by combining the snap-through behavior of inclined beams and the support of folded beams, acting as negative-stiffness (NS) and positive-stiffness (PS) elements, respectively. Analytical methods are developed for predicting the stiffness of the NS and PS elements of the design, whose efficacy is demonstrated numerically and experimentally through examining the static behavior. To evaluate the vibration isolation performance of the QZS isolator, a nonlinear single-degree-of-freedom (SDOF) model is proposed. The model incorporates cubic nonlinear damping in addition to classical viscous damping. The harmonic balance method (HBM) and the Runge-Kutta algorithm are employed to solve the equation of motion and to predict the velocity transmissibility. Parametric analyses are conducted to assess the effect of the excitation amplitude on isolation performance. The results show that an increased excitation level entails a downshifting of the peak frequency in the transmissibility curve and that of the starting frequency of the effective isolation zone, resulting in enhanced isolation performance at large amplitudes. Numerical findings are further supported by dynamic experiments with varying excitation levels, demonstrating the validity of the proposed numerical model.

1. Introduction

1.1. Background and motivation

Quasi-zero-stiffness (QZS) vibration isolators, with their unique high-static and low-dynamic stiffness features, show great promise for the design of vibration isolation devices to deliver effective vibration isolation in a much lower frequency range than their linear counterparts. Linear isolators are effective typically starting from frequencies exceeding $\sqrt{2}$ times the natural frequency of the isolator [1,2]. Thus, reducing stiffness would allow low-frequency isolation with a wider isolation range, at the expenses of generating larger static deformation and compromised system instability [2,3]. To overcome these challenges, QZS mechanisms can be exploited to

^{*} Corresponding author.

E-mail address: lucien.yu@polyu.edu.hk (X. Yu).

<https://doi.org/10.1016/j.jsv.2024.118308>

Received 24 October 2023; Received in revised form 15 January 2024; Accepted 23 January 2024

Available online 1 February 2024

0022-460X/© 2024 Elsevier Ltd. All rights reserved.

achieve high static stiffness (to support large static loads) and low dynamic stiffness (to widen the frequency range of isolation). This unique combination makes the QZS isolator a viable and attractive solution for low-frequency isolations.

QZS mechanisms are typically achieved by combining positive stiffness (PS) and negative stiffness (NS) elements in parallel to create competing stiffness effects to eventually achieve an overall QZS effect. Conventional way to design NS elements relies on horizontally and obliquely orientated springs [3–10]. For example, Carrella et al. [2] analyzed the static characteristics of a QZS system comprising a vertical spring in parallel with two oblique springs, demonstrating that the force-displacement relationship could be approximated by a cubic equation, which has since then been widely adopted in subsequent studies. Carrella et al. [11,12] further investigated the dynamics of the same QZS system and derived approximate expressions for the maximum transmissibility and jump-down frequency in the case of light damping. A variety of prototypes have been developed and experimentally tested, providing supporting evidence for the superior performance of QZS isolators compared to traditional linear ones [13–15]. To provide tunable nonlinear stiffness, Gatti [16] proposed an adjustable device comprising two pairs of linear oblique springs, whose geometric arrangement can be adjusted to achieve specific nonlinear force-displacement characteristics. Apart from oblique springs, NS mechanisms can also be achieved through other designs, such as magnets [17–20], inclined and curved beams [21–24], bistable plates and shells [25–27], cam rollers [28–30], scissor-like structures [31,32], metamaterial and origami-based structures [33–37], etc.

Given the difficulties in miniaturizing and implementing spring mechanisms of a tiny size while maintaining the dynamic property, continuous QZS structures based on compliant mechanisms would be more appropriate for protecting small-scale machines from external disturbance. Moreover, with the rapid development of additive manufacturing technology, customized continuous structures with integrated components can be conveniently manufactured via 3D printing. Several continuous QZS structures have been realized based on two generic design strategies. The first strategy combines the snap-through behavior of inclined beams and the support of curved beams, acting as NS and PS elements, respectively [38,39]. The second strategy employs a monolithic curved beam with tactically tuned geometric configurations [40–43]. Comparing these two strategies, the second approach yields more compact and integrated structures by avoiding the assembly of separate PS and NS elements. However, a significant drawback is that a careful tuning of the geometric parameters is required, as monolithic curved beams exhibit the NS property over a much wider parameter range than the QZS property [44]. Extensive geometric tuning to obtain the desired QZS property is usually conducted by characterizing the shape of monolithic curved beams using B-splines and polynomials [40–43]. The first strategy, which combines NS and PS elements together, offers the advantage of higher static stiffness and loading capacity along with a larger design space than the monolithic curved beam. As to the first strategy, Fan et al. [45] proposed a structure exhibiting QZS behavior and numerically investigated its vibration isolation performance in linear regime by arranging a sinusoidal beam and a couple of semicircular arches inside a stiffer frame. Based on Duffing's equation and the harmonic balance method (HBM), Dalela et al. [46] investigated the nonlinear behavior of a similar structure.

A limitation of conventional QZS systems is their hardening behavior, which can narrow the isolation region at high vibration amplitudes. To mitigate this, QZS systems can be optimized to extend the QZS range [6,47]. Apart from structural optimization, nonlinear inertia can reconcile the hardening behavior of a QZS isolator, which further reduces the starting isolation frequency [48]. In [49], external dampers were intentionally introduced to a QZS isolator consisting of springs, and the results indicated that, due to the additional dampers, the starting isolation frequency was shifted to lower frequencies as the excitation amplitudes increased. It can then be surmised that the significant damping effect, inherent in the soft materials, could provide a direct and simple solution to alleviate the adverse effects of the hardening behavior. This, however, has not been fully exploited in existing literature on continuous QZS structures.

Indeed, while there exist several studies on continuous QZS structures for vibration isolation [40,41,45,46,50], comprehensive analyses considering the nonlinear behavior and damping effects are scarce. Linear assumptions were adopted in [45], and the research was limited to the small-amplitude regime. Some research analytically investigated the influence of nonlinear stiffness on vibration isolation performance but relied on a linear viscous damping model [40,46]. However, when it comes to continuous QZS structures constructed with soft materials, a linear viscous damping model is insufficient to capture the complicated and substantial damping effects from internal friction. The work in [50] analytically explored the isolation performances of a QZS isolator fabricated with thermoplastic polyurethanes (TPU) using various damping models, but experimental investigation was not provided.

1.2. Objective and main contributions

This paper presents the design of a novel vibration isolator with embedded QZS properties that can be conveniently 3D printed with soft resins. The primary objective is to effectively counteract the adverse effects of the hardening behavior of conventional QZS isolators by leveraging the significant damping effects arising from the soft resin. As such, the starting isolation frequency of the proposed isolator is expected to shift to a lower frequency as the excitation amplitude increases, alongside a broadening of the isolation region. The main contributions of this paper to the existing literature on compliant QZS isolators can be summarized as follows:

- (1) A novel QZS isolator that can be easily fabricated by 3D printing using soft resins is proposed. The desired low-frequency isolation performance and robustness against excitation levels are showcased and experimentally validated.
- (2) Nonlinear damping, in addition to the classical viscous one, is introduced in the mechanical model to characterize the damping effect of soft resins, and the model is also validated by experiments.

The paper is organized as follows. Section 2 describes the proposed design of the QZS isolator. Experimental measurements and numerical analysis of the static force-displacement behavior of the designed isolator are presented in Section 3. In Section 4, a

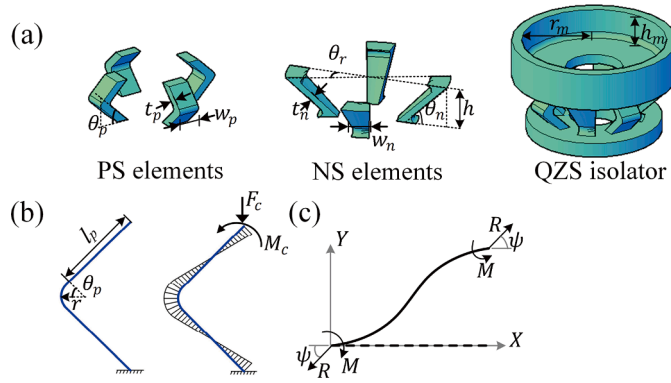


Fig. 1. Schematic illustration of (a) the proposed QZS isolator accompanied with its negative-stiffness (NS) and positive-stiffness (PS) elements, (b) free-body diagram and bending-moment diagram of the PS element, and (c) free-body diagram of the NS element [51].

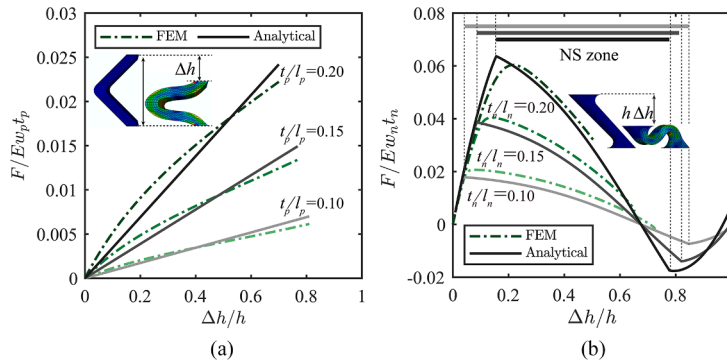


Fig. 2. Force-displacement curves obtained by the analytical method and finite element method (FEM) for folded and inclined beams with different thickness-to-length ratios: (a) PS elements and (b) NS elements. The corresponding negative-stiffness (NS) zones are indicated in Fig. 2b.

hardening single-degree-of-freedom (SDOF) model with nonlinear damping is developed. In Section 5, dynamic experiments are conducted to assess the isolation performance of the proposed QZS isolator and to validate the model. Conclusions are presented in Section 6.

2. The design and the static analysis of the QZS system

The proposed QZS isolator consists of two pairs of inclined beams acting as NS elements and two pairs of folded beams as PS elements, as schematically shown in Fig. 1. The inclined beams are designed to feature snap-through buckling behavior when subjected to compressive load, which provides negative stiffness and counteracts the positive stiffness of the folded beams. A platform is integrated at the top of the QZS mount to hold external payloads. The key parameters of the inclined beams, including the revolve angle θ_r , inclination angle θ_n , and thickness t_n , are depicted in Fig. 1(a). Since the beam width of the inclined beam is not constant along the beam length, its width w_n is estimated as the width at the middle height. Each folded beam is composed of two segments of beams with the same thickness t_p , width w_p , and inclination angle θ_p .

2.1. Analytical solutions for positive-stiffness and negative-stiffness elements

The positive stiffness of the folded beams at small deformation can be estimated by the Castigliano's theorem based on strain energy [38]. More precisely, the strain energy of these two folded beams can be written as

$$U = 2 \left(\int_0^{l_p} \frac{(M_c - F_c l_p \cos(\theta_p))^2}{2EI} ds + \int_0^{\theta_p} \frac{(M_c - F_c l_p \cos(\theta_p) - r \cos(\frac{\pi}{4} - \theta))^2}{2EI} r d\theta \right), \quad (1)$$

where M_c and F_c are the bending moment and axial force, respectively, as shown in Fig. 1(b). According to the Castigliano's theorem, the vertical displacement Δh , as depicted in Fig. 2, can be calculated by differentiating the strain energy U with respect to the force F_c , yielding

Table 1
Geometric parameters.

Geometric parameters	Value	Geometric parameters	Value	Geometric parameters	Value
θ_r (°)	25.0	θ_p (°)	45.0	r_m (mm)	15.0
θ_n (°)	45.0	t_p (mm)	0.5	h_m (mm)	6.0
t_n (mm)	0.5	w_p (mm)	4.0	w_n (mm)	4.2
l_n (mm)	9.5	l_p (mm)	6.0	h (mm)	10.0

Table 2
Mechanical properties of the resin (the 3D-printing material).

Material	E (MPa)	ρ (kg/m ³)	ν
Flexible resin	8.15	1150	0.42

$$\Delta h = \frac{\partial U}{\partial F_c} = \frac{1}{12EI} \left(24\sqrt{2}r^2 \left(F_c l_p \cos(\theta_p) - \frac{1}{2}M_c \right) + 6l_p^2 F_c \cos(\theta_p)^2 \left(\pi r + \frac{4}{3}l_p \right) - 6M_c l_p (\pi r + 2l_p) \cos(\theta_p) + 3F_c r^3 (\pi + 2) \right). \quad (2)$$

By introducing the boundary condition that the slope of the folded beam at the starting end is zero, an additional equation is established, i.e.,

$$\theta_c = \frac{\partial U}{\partial M_c} = \frac{1}{2EI} \left(M_c (\pi r + 4l_p) - 2\sqrt{2}F_c r^2 - F_c l_p (\pi r + 2l_p) \cos(\theta_p) \right) = 0. \quad (3)$$

Solving Eqs. (2) and (3) gives the relationship between F_c and Δh , which, when $\theta_p = \pi/4$, becomes:

$$F_c = k_p \Delta h, \quad (4)$$

where

$$k_p = \frac{12(\pi r + 4l_p)EI}{3\pi^2 r^4 + 4\pi l_p^3 r + 12\pi l_p r^3 + 6\pi r^4 + 4l_p^4 + 48l_p^2 r^2 + 24l_p r^3 - 48r^4} \quad (5)$$

is the stiffness of one PS element.

The NS element is a inclined fixed-guided beam, which is fixed at one end and the other end goes through a deflection such that the angular deflection at the end remains constant [51]. The deflection of the beam is antisymmetric about the center, as shown in Fig. 1 (c), and its negative stiffness can be determined from the load-displacement curves using the elliptic integral method under large deformation. Details can be found in [51,52].

2.2. Finite element modelling

To verify the analytical solution, three-dimensional (3D) finite element models (FEMs) of the PS and NS elements are established, respectively, as shown in Fig. 2. The dimensions of the FEMs are listed in Table 1. The geometrical mesh of the NS elements is constructed with the ten-node quadratic tetrahedron elements (C3D10), and that of the PS elements with the eight-node linear hexahedron elements (C3D8R). The mechanical properties of the linear elastic material model used are tabulated in Table 2. Geometrical nonlinearity is considered for the buckling behavior of the inclined beams. Moreover, self-contact interactions are defined to model contact interactions between different surfaces during compression.

2.3. Parametric studies on beam thickness

Fig. 2(a) presents the force-displacement curves for the folded beams with various thickness-to-length ratios, obtained by the FEM and the analytical method described in Section 2.1. The analytical results generally agree well with the FE results for the PS elements, although the analytical curves are linear while the FE curves are nonlinear. Therefore, the analytical model provides a reasonable estimate of the overall stiffness and can be used as a useful tool to provide design guidelines. The stiffness of the PS elements increases with thickness, through inspecting the trends in both the analytical and FE results.

As for the NS elements, as shown in Fig. 2(b), the analytical predictions exhibit good agreement with the FE results, although the convergence issues result in truncated force-displacement curves in the FE analysis. The snap-through phenomenon is clearly captured, with the restoring forces initially reaching a peak value before abruptly diving into a valley. Within the displacement range between the peak and valley, the NS property is achieved. Both the absolute value of the negative stiffness and the load-bearing capacity increase with the beam thickness. The displacement range of negative stiffness becomes narrower as a trade-off.

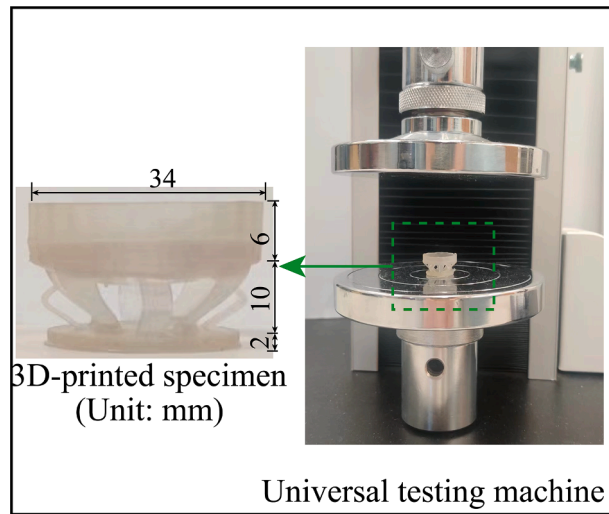


Fig. 3. A QZS sample printed using Flexible 80A Resin on the universal testing machine used for the quasi-static compression experiments.

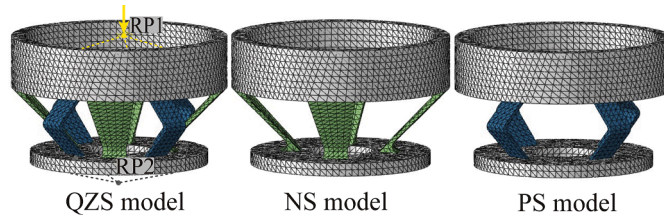


Fig. 4. Finite element models of a QZS isolator, its corresponding negative-stiffness (NS) and positive-stiffness (PS) elements.

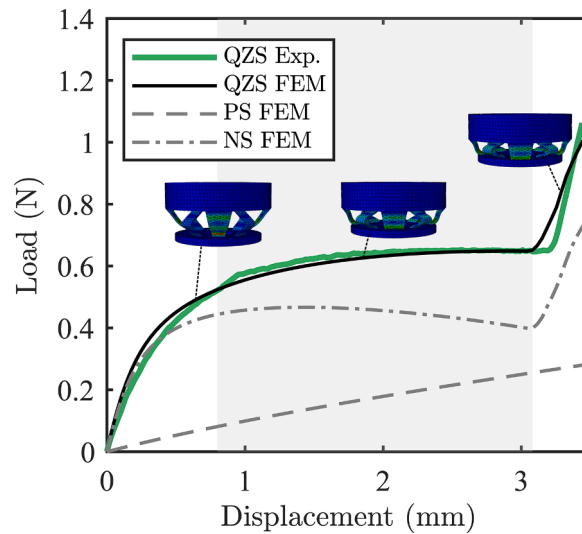


Fig. 5. Force-displacement curves of the QZS isolator produced through experiments (Exp.) and FEM, together with representative deformations at various stages. The restoring force-displacement curves of the corresponding PS and NS elements are also included.

3. Static characteristics of the QZS isolator

In this section, the static characteristics of the QZS isolator are investigated through quasi-static compression experiments and finite element simulations, and the measured force-displacement curves are used to reveal the desired QZS properties.

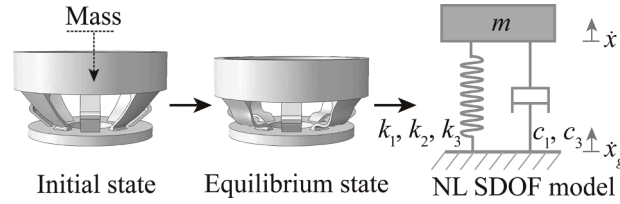


Fig. 6. Schematic models of the QZS isolator at initial and equilibrium states and the corresponding equivalent nonlinear (NL) SDOF dynamic model.

3.1. Quasi-static compression experiments

Samples of the proposed QZS isolator were fabricated by stereolithography (SLA) using a 3D printer, Formlabs Form 3+. Flexible 80A Resin was used, which can balance the softness with strength. An example of the printed sample is shown in Fig. 3, with the corresponding geometric parameters listed in Table 1. The fillet radii at the ends of the inclined beams and the corners of the folded beams were set to one millimeter.

To investigate the mechanical behavior of the QZS isolator, quasi-static compression tests were performed using a universal testing machine, as shown in Fig. 3. The compression test was performed under displacement control, with a loading rate of 0.1 mm per second.

3.2. Finite element simulation

To gain further insights into the mechanical behavior of the isolator, FE analyses are conducted in addition to the experimental investigation. As shown in Fig. 4, the QZS isolator is modeled by the ten-node quadratic tetrahedron element (C3D10). Similarly, a linear material model, with the material mechanical properties listed in Table 2, is applied. The bottom and top surfaces of the QZS are coupled to a reference point, respectively. The bottom reference point (RP2) is constrained in all six degrees of freedom, and a vertically prescribed displacement is applied at the top reference point (RP1) to simulate the compression process. For illustration of the contribution of the PS and NS elements, corresponding FEMs are also established, as shown in Fig. 4.

3.3. Static force-displacement curves

The measured restoring forces with respect to the displacement from both experimental results and FE analysis are displayed in Fig. 5, alongside representative deformations at different stages. Obviously, a platform region appears on the restoring force curve in the displacement range from 0.8 mm to 3.1 mm, typical of QZS behavior. Subsequently, the restoring force increases rapidly due to self-contact. The restoring force-displacement curves of the folded beams (PS elements) and the inclined beams (NS elements) are also shown in Fig. 5. The restoring force of the PS element increases monotonically with displacement, while that of the NS element rises steeply at first and then decreases suddenly due to the snap-through buckling of the inclined beams. As the QZS isolator embraces both the PS and NS elements, its behavior is a combination of these two types of elements.

4. System modelling and parameter identification

To understand the dynamic characteristics of the QZS system, an SDOF model incorporating nonlinear restoring force is established in this section. Two methods, including the harmonic balance method (HBM) and the 4th Runge-Kutta method, are used to solve the equation of motion (EOM) to derive the velocity transmissibility. A genetic algorithm is proposed for identifying model parameters from dynamic experiments.

4.1. Single-degree-of-freedom models

The proposed continuous QZS mount can be modelled using an SDOF nonlinear model, as shown in Fig. 6. Geometric nonlinearities are included in a modified Duffing equation in which a quadratic stiffness term is added to account for the asymmetry due to friction, curvature, or imperfection [53]. Thus, the elastic restoring force of the spring is modeled by a three-order polynomial $F_e = k_1x + k_2x^2 + k_3x^3$, where x is the displacement of the mass and k_1 , k_2 and k_3 are the linear, quadratic, and cubic stiffness coefficients, respectively.

For continuous structures, studies revealed a nonlinear evolution of damping, usually an increase with large amplitudes of oscillation [53]. Therefore, the linear damping model employed in the literature on continuous QZS structures [40,46] should be replaced by a nonlinear damping model. The choice of functional form for nonlinear damping is a tricky task [54,55]. Various expressions in the form of polynomials in terms of velocity \dot{x} , from the quadratic up to the cubic, have been proposed [53]. Based on preliminary studies, the nonlinear damping of the type $c_1\dot{x} + c_3x^2\dot{x}$, where c_1 and c_3 are the linear and cubic damping coefficients, respectively, is chosen in this study.

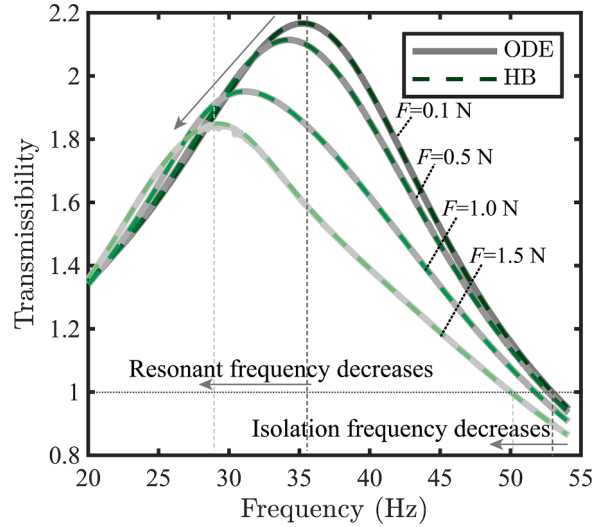


Fig. 7. The evolution of velocity transmissibility with various excitation amplitudes. Model parameters in Table 4 are employed in the simulation for illustration.

For a harmonic base displacement excitation, $x_g = X_g \cos(\omega t)$, the equation of motion (EOM) of the system is written as:

$$m\ddot{x} + c_1\dot{x} + c_3x^2\dot{x} + k_1x + k_2x^2 + k_3x^3 = m\omega^2 X_g \cos(\omega t), \quad (6)$$

where m is the mass, ω and X_g are the circular frequency and amplitude of the excitation, respectively. With all nonlinear internal force terms regrouped into $f_{int}(x, \dot{x})$ and the external force denoted by $f_{ext}(\omega, t) = F \cos(\omega t)$, the EOM is cast into the following general form,

$$m\ddot{x} + c_1\dot{x} + k_1x + f_{int}(x, \dot{x}) = f_{ext}(\omega, t). \quad (7)$$

4.2. Numerical methods for solving system equation

Equation (7) can be numerically solved using the HBM. The relative displacement x and the resultant force $f = f_{ext}(\omega, t) - f_{int}(x, \dot{x})$ are then approximated by Fourier series truncated to the N^{th} -harmonic as,

$$x(t) = q_0^x + \sum_{k=1}^N (q_{k_s}^x \sin(k\omega t) + q_{k_c}^x \cos(k\omega t)), \quad (8)$$

and

$$f(t) = q_0^f + \sum_{k=1}^N (q_{k_s}^f \sin(k\omega t) + q_{k_c}^f \cos(k\omega t)), \quad (9)$$

where q_{k_s} and q_{k_c} denote the k^{th} -harmonic Fourier coefficients related to the sine and cosine terms, respectively. The Fourier coefficients of $f(t)$ depend on the Fourier coefficients of the displacement $x(t)$, which represent the new unknowns of the problem. These coefficients are gathered into $2N + 1 \times 1$ vectors,

$$\mathbf{z} = [q_0^x, q_{1_s}^x, q_{1_c}^x, \dots, q_{N_s}^x, q_{N_c}^x]^T, \quad (10)$$

$$\mathbf{b} = [q_0^f, q_{1_s}^f, q_{1_c}^f, \dots, q_{N_s}^f, q_{N_c}^f]^T. \quad (11)$$

Substituting Eqs. (8-11) into Eq. (7) and following the standard Fourier-Galerkin balance procedure, the EOM expressed in the frequency domain is eventually obtained in a compact form [56,57],

$$\mathbf{h}(\mathbf{z}, \omega) = \mathbf{A}(\omega)\mathbf{z} - \mathbf{b}(\mathbf{z}) = 0, \quad (12)$$

where $\mathbf{A} = \nabla^2 \otimes \mathbf{M} + \nabla \otimes \mathbf{C} + \mathbf{I}_{2N+1} \otimes \mathbf{K}$ is the matrix for linear system; \otimes stands for the Kronecker tensor product; ∇ and ∇^2 are gradient and Laplace operator matrices defined in [56]. Equation (12) is nonlinear and should be solved iteratively. The Newton-Raphson method and the Moore-Penrose continuation method are utilized to reach the final solution.

Equation (7) can also be numerically integrated by the Runge-Kutta method. The results obtained by the HBM and the Runge-Kutta method are compared in Appendix to validate numerical methods, in which the harmonic truncation order N is investigated.

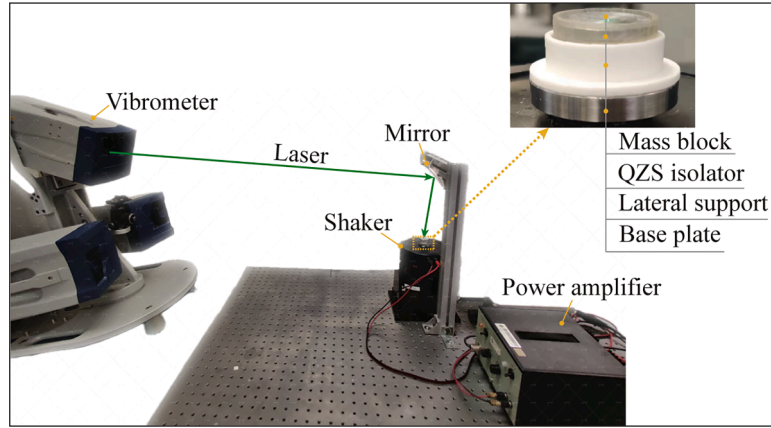


Fig. 8. Experimental set-up for transmissibility of the QZS isolator. The laser beam of the vibrometer was redirected by a mirror to measure the vertical velocity responses of the mass block and the base plate fixed at the top of the shaker.

The influence of excitation amplitudes on the performance of the QZS isolator is discussed numerically by using the validated HB method and the Runge-Kutta method. The evolution of the velocity transmissibility with various excitation amplitudes is presented in Fig. 7. As the excitation amplitude rises, the peak frequency and the starting isolation frequency gradually move to the lower frequency region, alongside a decrease of the peak value. As a result, the isolation performance is improved at higher excitation levels compared to smaller ones.

4.3. Parameter identification using genetic algorithm

This section deals with the parameter identification of the SDOF model in Fig. 6 by matching available experimental data. The procedure to estimate model parameters is split into two successive processes. First, as a prerequisite for nonlinear identification, the linear stiffness coefficient is estimated using the frequency responses in a small-amplitude regime. Then, SDOF system is solved using the Runge-Kutta method and the remaining parameters of the system are estimated by minimizing the differences between the numerical and experimental data using a genetic algorithm. The difference between experimental and numerical responses is measured using the root mean squared error (RMSE) as shown in Eq. (13),

$$\text{RMSE} = \sqrt{\frac{\sum_{i=1}^{N_f} (\hat{y}_i - y_i)^2}{N_f}}, \quad (13)$$

where $y_i = v_i/v_{b_i}$ and $\hat{y}_i = \hat{v}_i/v_{b_i}$ represent the experimental and numerical transmissibility (y_i and \hat{y}_i) obtained by normalizing the experimentally and numerically obtained steady velocity amplitude (v_i and \hat{v}_i) by the base velocity amplitude v_{b_i} at a discrete frequency f_i , respectively. N_f denotes the number of discrete frequencies employed for system parameter estimation.

Then, to estimate the system parameter, the optimization problem towards minimization of RMSE is conducted by means of the global search genetic algorithm implemented in MATLAB routine *ga*, detailed as follows:

Find

$$\mathbf{d} = [\eta_2, \eta_3, \gamma_1, \gamma_3], \quad (14)$$

to minimize RMSE, when subjected to

$$d_i^L \leq d_i \leq d_i^U \quad (i = 1, \dots, 4), \quad (15)$$

where \mathbf{d} is a vector consisting of four system parameters; $\eta_2 = -\frac{1}{10^5} \frac{k_2}{k_1}$ and $\eta_3 = \frac{1}{10^6} \frac{k_3}{k_1}$ denote the quadratic and cubic dimensionless stiffness coefficients, respectively; $\gamma_1 = \frac{c_1}{20}$ and $\gamma_3 = \frac{1}{10^2} \frac{c_3}{c_1}$ are the linear and cubic dimensionless damping coefficients, respectively. Additionally, d_i^L and d_i^U represent the lower and upper bound of each normalized system parameter, which are zero and one in the normalized space, respectively.

Apart from RMSE in Eq. (13), the coefficient of determination (R^2) defined in Eq. (16), is also introduced to assess the discrepancy between the experimental and numerical results with the estimated system parameters.

$$R^2 = 1 - \frac{\sum_{i=1}^{N_f} (\hat{y}_i - y_i)^2}{\sum_{i=1}^{N_f} (y_i - \bar{y})^2} \quad (16)$$

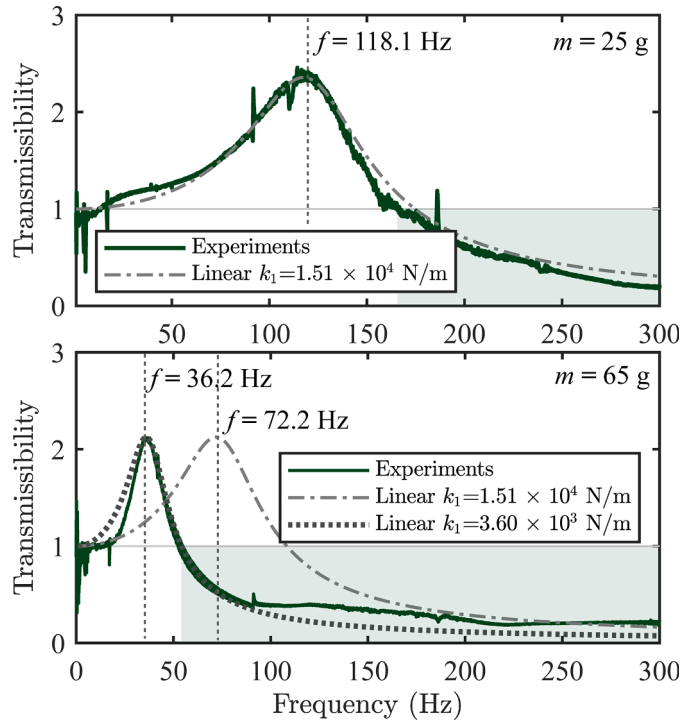


Fig. 9. Comparison between experimental and analytical results of transmissibility at the small-amplitude excitation of 1 V. The upper and lower subplot are the results for $m = 25$ g case and $m = 65$ g case, respectively.

5. Dynamic Experiments

Dynamic experiments were conducted with the twofold aim of investigating the isolation behavior of the proposed QZS isolator and validating the numerical model employed. The experimental set-up and procedures are to be addressed in this section.

5.1. Experimental set-up

The experimental set-up of the vibration measurement is illustrated in Fig. 8. An electrodynamical shaker, model B&K 4810, was used to provide excitation. A base plate was fixed on the shaker, on the top of which was the fixed printed sample. Due to the unavoidable initial geometric imperfection from the 3D printing, which leads to eccentric loading, a tube with an inner diameter one millimeter larger than the outer diameter of the platform was installed outside of the platform to provide lateral support for the QZS isolator, as shown in Fig. 8. Lubricant was applied to both the inner surface of the tube and the outer surface of the QZS isolator to reduce the friction between the two parts. The outer tube was printed with polylactic acid (PLA) using a fused deposition modelling (FDM) 3D printer.

The velocity responses were measured using a laser Doppler vibrometer (Polytec PSV 500). The laser beam was redirected by a mirror to measure the vertical velocity response, as shown in Fig. 8. To extract the velocity transmissibility, the velocity of the mass block and that of the base plate were measured using the laser vibrometer.

5.2. Experimental procedure

From the static experimental results shown in Fig. 5, the 3D printed sample of QZS isolator reaches the QZS zone with a payload of around 65 grams. Thus, a mass block weighing 65 grams was fixed at the top of the isolator to investigate its QZS property. For comparison, a mass block weighing 25 grams was chosen to exhibit the property of the isolator before it reaches the QZS zone.

Usually, for the convenience of presenting experimental results, closed-loop control is used in swept-sine tests to keep the amplitude of the harmonic force constant while varying the excitation frequency [58]. However, in this paper, the excitation amplitude was directly controlled and measured using voltage. First, small-amplitude swept-sine tests were performed for both $m = 25$ g and $m = 65$ g. The excitation frequency was increased from 1 Hz to 300 Hz in 102.4 seconds to find the fundamental frequency for each case. Then, for the $m = 65$ g case, experiments were performed by increasing the excitation frequency from 5 Hz to 95 Hz in 102.4 seconds, which covers the neighborhood of the fundamental natural frequency. Five different voltage levels were deployed to investigate the isolation performance under different excitation levels. It is worth noting that the sweep rate is determined by comparing the envelop of swept-sine responses to the single-frequency response at multiple frequencies to ensure that the sweep rate is slow enough to obtain

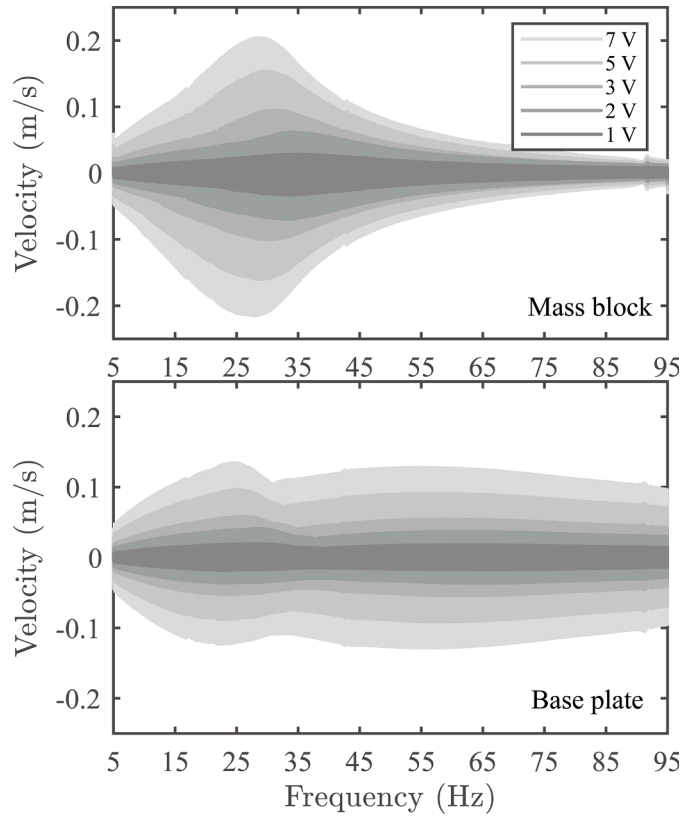


Fig. 10. Velocity responses of the mass block (upper subplot) and the base plate (lower subplot) at five different excitation levels.

steady-state responses.

6. Results and Discussion

In this section, the performance of the proposed QZS isolator is first evaluated through comparisons with the linear isolator based on experimental results at small amplitudes. Then, the influence of excitation amplitude on the isolation performance is discussed. The proposed SDOF model and the parameter identification procedure are validated by comparing the experimental and numerical results.

6.1. Vibration isolation performance at small amplitudes

The velocity transmissibility is first extracted from the small-amplitude experimental results. For the case of $m = 25$ g, the linear stiffness of the isolator before reaching the QZS range is estimated by fitting the experimental results with linear analytical transmissibility, which is shown in Eq. (17) [40],

$$T = \frac{\sqrt{1 + \left(2\xi \frac{\omega}{\omega_n}\right)^2}}{\sqrt{\left(1 - \left(\frac{\omega}{\omega_n}\right)^2\right)^2 + \left(2\xi \frac{\omega}{\omega_n}\right)^2}} \quad (17)$$

where $\omega_n = \sqrt{k_1/m}$ and $\xi = c_1/2m\omega_n$. The comparison between the experimental and analytical results is presented in the upper subplot in Fig. 9. With an estimated linear stiffness k_1 of 1.51×10^4 N/m and a linear damping ratio ξ of 0.24, the analytical results match the experimental results. The peak frequency and the starting isolation frequency are 118.1 Hz and 165.6 Hz, respectively.

When the mass is increased to 65 g, the peak frequency shifts from 118.1 Hz to 36.2 Hz, and effective isolation starts to be achieved at 54.1 Hz, as shown in the lower subplot in Fig. 9. If the stiffness of the isolator remains unchanged while the mass increases from 25 g to 65 g, the theoretical transmissibility is shown as the dash-dotted line with a peak frequency of 72.2 Hz, which is much higher than that of the experimental results. Moreover, by fitting the experimental results with the linear analytical results, the stiffness in this case is estimated at 3.60×10^3 N/m, which is only 23.8% of the stiffness in the case of $m = 25$ g. By far, the experimental results indicate that the designed isolator materializes the desired QZS property and thus reaches a lower isolation frequency compared with the

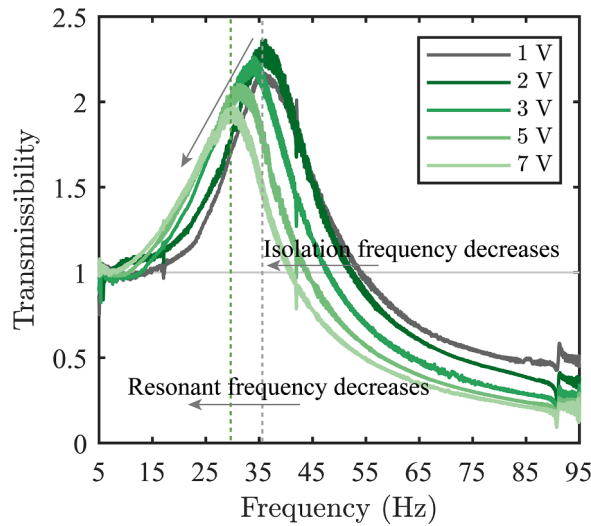


Fig. 11. Velocity transmissibility at five different excitation levels.

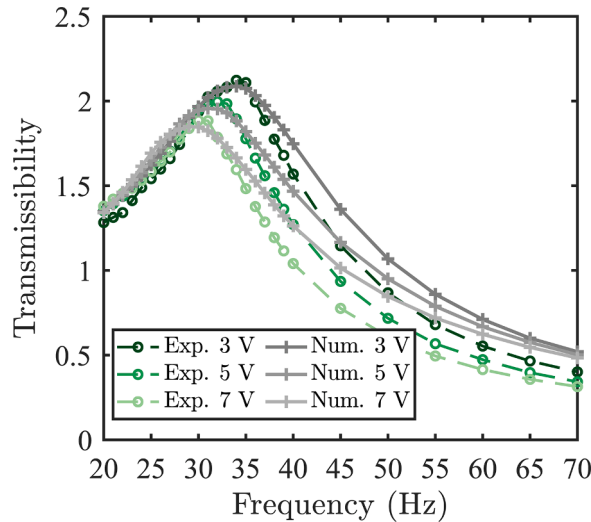


Fig. 12. Experimental and numerical acceleration transmissibility of the QZS isolator for three excitation amplitudes.

Table 3
Optimized results of the normalized parameters.

Parameter	η_2	η_3	γ_1	γ_3
Value	0.012	0.543	0.409	0.385

corresponding linear isolator.

6.2. Vibration isolation performance at different amplitudes

The measured velocity responses of the mass block and the base plate at five different excitation levels, namely 1 V, 2 V, 3 V, 5 V, and 7 V, are displayed in the upper and lower subplots of Fig. 10, respectively. Fig. 11 presents the corresponding velocity transmissibility. As the excitation level increases from 2 V to 7 V, both the peak frequency and the starting isolation frequency are downshifted, alongside a gradual decrease in the resonant amplitudes. Thus, the isolation performance is better at higher excitation levels than lower excitation levels. These experimental results also confirm the HBM-predicted observation in Fig. 7. In summary, the design objective of utilizing the large damping effect of the soft resin to neutralize the detrimental effects of the hardening behavior of

Table 4
Parameters for the optimized numerical model.

Parameter	k_1 (N/m)	k_2 (N/m ²)	k_3 (N/m ³)	c_1 (N/(m/s))	c_3 (N/(m ³ /s))
Value	3.60×10^3	-4.32×10^6	1.95×10^9	8.18	314.48

Table 5
Performance of the optimized model for response predictions.

Excitation level	RMSE	R ²	Peak frequency ratio (Numerical/test)	Peak amplitude ratio (Numerical/test)
3V	0.111	0.953	1.000	0.983
5V	0.122	0.940	0.969	0.980
7V	0.140	0.917	0.967	0.980

the QZS isolator to obtain better isolation performance at large amplitudes has been achieved.

6.3. Comparison of numerical and experimental results

The experimentally obtained transmissibility of multiple frequencies at three excitation levels is estimated from the envelopes of the swept-sine responses shown in Fig. 10. The experimental results are shown as circles in Fig. 12. Using these results and following the procedures in Section 4.3, the normalized parameters in Table 3 are obtained. The corresponding stiffness and damping parameters are displayed in Table 4. As shown in Fig. 12, the transmissibility curves from the numerical results are consistent with those from the experimental results. The two indices in Eqs. (13) and (16), accompanied by two additional indices, i.e., the peak frequency ratio and the peak amplitude ratio, are summarized in Table 5 to evaluate the difference between the numerical and experimental results. The results prove that the numerical model with the parameters shown in Table 4 is of high accuracy in modelling the system, as evidenced by the R² values exceeding 0.91 for all three excitation levels, and the maximum deviations within 5% for the peak frequency and peak amplitude. Thus, both the employed restoring force model and the parameter estimation procedure are validated.

7. Conclusion

In this paper, a continuous QZS isolator is proposed and implemented using 3D printing. The required QZS properties are achieved by combining the snap-through behavior of inclined beams and the support of folded beams, acting as negative-stiffness (NS) and positive-stiffness (PS) elements, respectively. The static properties of the QZS isolator are thoroughly investigated through numerical simulations and experimental tests. The results show that the combination of NS and PS elements can lead to the desired QZS features.

To fully understand the dynamic performance of the QZS isolator, a nonlinear SDOF model is established, which incorporates a cubic damping model. Experimental tests are conducted to assess the isolation performance of the proposed device and verify the numerical findings, as evidenced by the observed agreement between them. Moreover, the velocity transmissibility obtained by the experimental and numerical results both indicate that the resonant peaks and the starting isolation frequency decrease with increasing excitation amplitudes, thus entailing better isolation performance at higher excitation levels, which is distinct from existing QZS isolators. This improvement is achieved by neutralizing the hardening effect of the QZS isolator with the significant damping effect of the soft resin.

In conclusion, the integrated isolator proposed in this paper effectively combines the QZS properties and the significant damping effects of the soft resin, to achieve superior isolation performance in the low-frequency range and robustness against the changes in the excitation levels. Future research is needed to explore structural optimization and inverse design methods to further improve the performance of the proposed QZS isolator.

Declaration of competing interest

The authors declare that they have no known competing financial interests or personal relationships that could have appeared to influence the work reported in this paper.

Acknowledgements

The work described in this paper was fully / substantially / partially supported by a grant from the NSFC/RGC Joint Research Scheme sponsored by the Research Grants Council of Hong Kong and the National Natural Science Foundation of China (Project No. N_PolyU553/23). The authors acknowledge the support from the Post-doctoral Matching Fund and the Start-up Fund of the Hong Kong Polytechnic University. The authors would like to thank Dr. Shuwei An and Mr. Yuanman Zhang—Department of Mechanical Engineering, The Hong Kong Polytechnic University—for their help in the experiments.

Appendix

Generally, the harmonic truncation order N should be selected as large as necessary to achieve the required accuracy and as small as possible to avoid spurious effort. Equation (7) is integrated by means of the 4th Runge-Kutta scheme using the Matlab solver *ode45* as a reference to select the appropriate truncation order. The results of the convergence study are illustrated in Fig. A.1. Obviously, good agreement between the HB predictions when $N = 5$ and the numerical simulations can be observed.

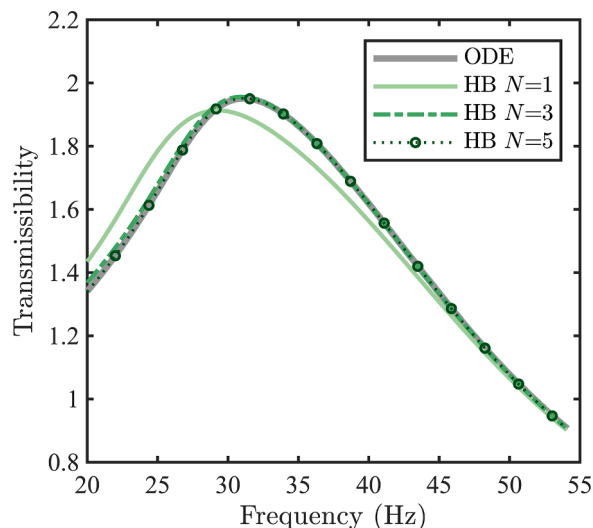


Fig. A.1. Convergence study on the harmonic truncation order N when $F=1.0 N$. Model parameters in Table 4 are employed in the simulation for illustration.

References

- [1] R. Ibrahim, Recent advances in nonlinear passive vibration isolators, *J. Sound. Vib.* 314 (3–5) (2008) 371–452.
- [2] A. Carrella, M. Brennan, T. Waters, Static analysis of a passive vibration isolator with quasi-zero-stiffness characteristic, *J. Sound. Vib.* 301 (3–5) (2007) 678–689.
- [3] I. Kovacic, M.J. Brennan, T.P. Waters, A study of a nonlinear vibration isolator with a quasi-zero stiffness characteristic, *J. Sound. Vib.* 315 (3) (2008) 700–711.
- [4] J. Zhou, L. Dou, K. Wang, D. Xu, H. Ouyang, A nonlinear resonator with inertial amplification for very low-frequency flexural wave attenuations in beams, *Nonlinear. Dyn.* 96 (1) (2019) 647–665.
- [5] H. Ding, J. Ji, L.-Q. Chen, Nonlinear vibration isolation for fluid-conveying pipes using quasi-zero stiffness characteristics, *Mech. Syst. Signal. Process.* 121 (2019) 675–688.
- [6] F. Zhao, J. Ji, K. Ye, Q. Luo, An innovative quasi-zero stiffness isolator with three pairs of oblique springs, *Int. J. Mech. Sci.* 192 (2021) 106093.
- [7] Q. Wang, J. Zhou, K. Wang, J. Gao, Q. Lin, Y. Chang, D. Xu, G. Wen, Dual-function quasi-zero-stiffness dynamic vibration absorber: low-frequency vibration mitigation and energy harvesting, *Appl. Math. Model.* 116 (2023) 636–654.
- [8] J. Zhou, D. Xu, S. Bishop, A torsion quasi-zero stiffness vibration isolator, *J. Sound. Vib.* 338 (2015) 121–133.
- [9] L. Xiao, M. Iqbal, X. Yu, Quasi-static band gaps in metamaterial pipes with negative stiffness resonators, *Int. J. Mech. Sci.* (2023) 108668.
- [10] L. Xiao, O.S. Bursi, M. Wang, S. Nagarajaiah, F. Sun, X.-L. Du, Metamaterial beams with negative stiffness absorbers and rotation: band-gap behavior and band-gap merging, *Eng. Struct.* 280 (2023) 115702.
- [11] A. Carrella, M. Brennan, I. Kovacic, T. Waters, On the force transmissibility of a vibration isolator with quasi-zero-stiffness, *J. Sound. Vib.* 322 (4–5) (2009) 707–717.
- [12] A. Carrella, M. Brennan, T. Waters, V. Lopes Jr, Force and displacement transmissibility of a nonlinear isolator with high-static-low-dynamic-stiffness, *Int. J. Mech. Sci.* 55 (1) (2012) 22–29.
- [13] C.-C. Lan, S.-A. Yang, Y.-S. Wu, Design and experiment of a compact quasi-zero-stiffness isolator capable of a wide range of loads, *J. Sound. Vib.* 333 (20) (2014) 4843–4858.
- [14] D. Xu, Y. Zhang, J. Zhou, J. Lou, On the analytical and experimental assessment of the performance of a quasi-zero-stiffness isolator, *J. Vib. Control* 20 (15) (2014) 2314–2325.
- [15] T.D. Le, K.K. Ahn, A vibration isolation system in low frequency excitation region using negative stiffness structure for vehicle seat, *J. Sound. Vib.* 330 (26) (2011) 6311–6335.
- [16] G. Gatti, An adjustable device to adaptively realise diverse nonlinear force-displacement characteristics, *Mech. Syst. Signal. Process.* 180 (2022) 109379.
- [17] Q. Wang, J. Zhou, D. Xu, H. Ouyang, Design and experimental investigation of ultra-low frequency vibration isolation during neonatal transport, *Mech. Syst. Signal. Process.* 139 (2020) 106633.
- [18] Y. Chang, J. Zhou, K. Wang, D. Xu, A quasi-zero-stiffness dynamic vibration absorber, *J. Sound. Vib.* 494 (2021) 115859.
- [19] Y. Chang, J. Zhou, K. Wang, D. Xu, Theoretical and experimental investigations on semi-active quasi-zero-stiffness dynamic vibration absorber, *Int. J. Mech. Sci.* 214 (2022) 106892.
- [20] Y. Zheng, X. Zhang, Y. Luo, Y. Zhang, S. Xie, Analytical study of a quasi-zero stiffness coupling using a torsion magnetic spring with negative stiffness, *Mech. Syst. Signal. Process.* 100 (2018) 135–151.
- [21] X. Tan, B. Wang, S. Chen, S. Zhu, Y. Sun, A novel cylindrical negative stiffness structure for shock isolation, *Compos. Struct.* 214 (2019) 397–405.
- [22] T.R. Giri, R. Mailen, Controlled snapping sequence and energy absorption in multistable mechanical metamaterial cylinders, *Int. J. Mech. Sci.* 204 (2021) 106541.

- [23] R. Gao, S. Guo, X. Tian, S. Liu, A negative-stiffness based 1D metamaterial for bidirectional buffering and energy absorption with state recoverable characteristic, *Thin-Walled Struct.* 169 (2021) 108319.
- [24] B. Chen, L. Chen, B. Du, H. Liu, W. Li, D. Fang, Novel multifunctional negative stiffness mechanical metamaterial structure: tailored functions of multi-stable and compressive mono-stable, *Composites Part B: Engineering* 204 (2021) 108501.
- [25] A. Shaw, S. Neild, D. Wagg, P. Weaver, A. Carrella, A nonlinear spring mechanism incorporating a bistable composite plate for vibration isolation, *J. Sound. Vib.* 332 (24) (2013) 6265–6275.
- [26] X. Tan, S. Zhu, B. Wang, K. Yao, S. Chen, P. Xu, L. Wang, Y. Sun, Mechanical response of negative stiffness truncated-conical shell systems: experiment, numerical simulation and empirical model, *Composites Part B: Engineering* 188 (2020) 107898.
- [27] J. Shi, H. Mofatteh, A. Mirabolghasemi, G. Desharnais, A. Akbarzadeh, Programmable multistable perforated shellular, *Adv. Mater.* 33 (42) (2021) 2102423.
- [28] M. Li, W. Cheng, R. Xie, A quasi-zero-stiffness vibration isolator using a cam mechanism with user-defined profile, *Int. J. Mech. Sci.* 189 (2021) 105938.
- [29] S. Zuo, D. Wang, Y. Zhang, Q. Luo, Design and testing of a parabolic cam-roller quasi-zero-stiffness vibration isolator, *Int. J. Mech. Sci.* 220 (2022) 107146.
- [30] K. Ye, J. Ji, T. Brown, Design of a quasi-zero stiffness isolation system for supporting different loads, *J. Sound. Vib.* 471 (2020) 115198.
- [31] Y. Xiong, F. Li, Y. Wang, A nonlinear quasi-zero-stiffness vibration isolation system with additional X-shaped structure: theory and experiment, *Mech. Syst. Signal. Process.* 177 (2022) 109208.
- [32] X. Chong, Z. Wu, F. Li, Vibration isolation properties of the nonlinear X-combined structure with a high-static and low-dynamic stiffness: theory and experiment, *Mech. Syst. Signal. Process.* 179 (2022) 109352.
- [33] H. Han, V. Sorokin, L. Tang, D. Cao, A nonlinear vibration isolator with quasi-zero-stiffness inspired by Miura-origami tube, *Nonlinear. Dyn.* 105 (2021) 1313–1325.
- [34] H. Han, V. Sorokin, L. Tang, D. Cao, Lightweight origami isolators with deployable mechanism and quasi-zero-stiffness property, *Aerosp. Sci. Technol.* 121 (2022) 107319.
- [35] K. Ye, J. Ji, An origami inspired quasi-zero stiffness vibration isolator using a novel truss-spring based stack Miura-ori structure, *Mech. Syst. Signal. Process.* 165 (2022) 108383.
- [36] Z. Zhai, Y. Wang, K. Lin, L. Wu, H. Jiang, In situ stiffness manipulation using elegant curved origami, *Sci. Adv.* 6 (47) (2020) eabe2000.
- [37] J.C. Ji, Q. Luo, K. Ye, Vibration control based metamaterials and origami structures: a state-of-the-art review, *Mech. Syst. Signal. Process.* 161 (2021) 107945.
- [38] C. Cai, J. Zhou, L. Wu, K. Wang, D. Xu, H. Ouyang, Design and numerical validation of quasi-zero-stiffness metamaterials for very low-frequency band gaps, *Compos. Struct.* 236 (2020) 111862.
- [39] S. Guo, R. Gao, X. Tian, S. Liu, A quasi-zero-stiffness elastic metamaterial for energy absorption and shock attenuation, *Eng. Struct.* 280 (2023) 115687.
- [40] J. Zhao, G. Zhou, D. Zhang, I. Kovacic, R. Zhu, H. Hu, Integrated design of a lightweight metastructure for broadband vibration isolation, *Int. J. Mech. Sci.* 244 (2023) 108069.
- [41] Q. Zhang, D. Guo, G. Hu, Tailored mechanical metamaterials with programmable quasi-zero-stiffness features for full-band vibration isolation, *Adv. Funct. Mater.* 31 (33) (2021) 2101428.
- [42] Q. Lin, J. Zhou, K. Wang, D. Xu, G. Wen, Q. Wang, C. Cai, Low-frequency locally resonant band gap of the two-dimensional quasi-zero-stiffness metamaterials, *Int. J. Mech. Sci.* 222 (2022) 107230.
- [43] C. Cai, J. Zhou, K. Wang, D. Xu, G. Wen, Metamaterial plate with compliant quasi-zero-stiffness resonators for ultra-low-frequency band gap, *J. Sound. Vib.* 540 (2022) 117297.
- [44] X. Tan, B. Wang, L. Wang, S. Zhu, S. Chen, K. Yao, P. Xu, Effect of beam configuration on its multistable and negative stiffness properties, *Compos. Struct.* 286 (2022) 115308.
- [45] H. Fan, L. Yang, Y. Tian, Z. Wang, Design of metastructures with quasi-zero dynamic stiffness for vibration isolation, *Compos. Struct.* 243 (2020) 112244.
- [46] S. Dalela, P. Balaji, D. Jena, Design of a metastructure for vibration isolation with quasi-zero-stiffness characteristics using bistable curved beam, *Nonlinear. Dyn.* 108 (3) (2022) 1931–1971.
- [47] F. Zhao, J.C. Ji, K. Ye, Q. Luo, Increase of quasi-zero stiffness region using two pairs of oblique springs, *Mech. Syst. Signal. Process.* 144 (2020) 106975.
- [48] G. Yan, J.-J. Lu, W.-H. Qi, T.-Y. Zhao, H. Yan, L.-C. Zhao, Z.-Y. Wu, W.-M. Zhang, Tetrahedron structure with nonlinear stiffness and inertia modulation for enhanced low frequency vibration isolation, *J. Sound. Vib.* (2023) 117897.
- [49] X. Hu, C. Zhou, The effect of various damping on the isolation performance of quasi-zero-stiffness system, *Mech. Syst. Signal. Process.* 171 (2022) 108944.
- [50] Y. Zheng, W.-B. Shangquan, X.-A. Liu, Modeling of a quasi-zero static stiffness mount fabricated with TPU materials using fractional derivative model, *Mech. Syst. Signal. Process.* 177 (2022) 109258.
- [51] Howell, L.L., S.P. Magleby, and B.M. Olsen, *Handbook of Compliant Mechanisms*.
- [52] Holst, G.L., G.H. Teichert, and B.D. Jensen, *Modeling and experiments of buckling modes and deflection of fixed-guided beams in compliant mechanisms*. 2011.
- [53] S. Le Guisquet, M. Amabili, Identification by means of a genetic algorithm of nonlinear damping and stiffness of continuous structures subjected to large-amplitude vibrations. Part I: single-degree-of-freedom responses, *Mech. Syst. Signal. Process.* 153 (2021) 107470.
- [54] S. Adhikari, J. Woodhouse, Identification of damping: part 1, viscous damping, *J. Sound. Vib.* 243 (1) (2001) 43–61.
- [55] S. Adhikari, J. Woodhouse, Identification of damping: part 2, non-viscous damping, *J. Sound. Vib.* 243 (1) (2001) 63–88.
- [56] T. Detroux, L. Renson, L. Masset, G. Kerschen, The harmonic balance method for bifurcation analysis of large-scale nonlinear mechanical systems, *Comput. Methods Appl. Mech. Eng.* 296 (2015) 18–38.
- [57] X. Sun, G. Kerschen, L. Cheng, Geometrical nonlinearities in a curved cantilever beam: a condensation model and inertia-induced nonlinear features, *Nonlinear. Dyn.* 111 (7) (2023) 6533–6556.
- [58] M. Amabili, Nonlinear damping in nonlinear vibrations of rectangular plates: derivation from viscoelasticity and experimental validation, *J. Mech. Phys. Solids.* 118 (2018) 275–292.